Article

Discovery of 6-(fluoro-*F*)-3-(1H-pyrrolo[2,3-c]pyridin-1-yl)isoquinolin-5-amine ([F]-MK-6240): A Positron Emission Tomography (PET) Imaging Agent for Quantification of Neurofibrillary Tangles (NFTs)

Abbas M. Walji, Eric D. Hostetler, Harold Selnick, Zhizhen Zeng, Patricia Miller, Idriss Bennacef, Cristian Salinas, Brett Connolly, Liza Gantert, Marie Holahan, Stacey O'Malley, Mona Purcell, Kerry Riffel, Jing Li, Jaume Balsells, Julie A. OBrien, Stacey Melquist, Aileen Soriano, Xiaoping Zhang, Aimie Ogawa, Serena Xu, Elizabeth M Joshi, Joseph Della Rocca, Fred J. Hess, Joel Schachter, David Hesk, David Schenk, Arie Struyk, Kerim Babaoglu, Talakad G Lohith, Yaode Wang, Kun Yang, Jianmin Fu, Jeffrey L. Evelhoch, and Paul J Coleman

Just Accepted

1
2
3
4
5
6
7
8
9
10
11
12
13
14
15
16
17
18
19
20
21
22
23
24
25
26
27
28
29
30
31
32
33
34
35
36
37
38
39
40
41
42
43
44
45
46
47
48
49
50
51
52
53
54
55
56
57
58
59
60

SCHOLARONE™
Manuscripts

Discovery of 6-(fluoro-^{18}*F*)-3-(1H-pyrrolo[2,3-c]pyridin-1-yl)isoquinolin-5-amine ([^{18}F]-MK-6240): A Positron Emission Tomography (PET) Imaging Agent for Quantification of Neurofibrillary Tangles (NFTs)

Abbas M. Walji*[a], Eric D. Hostetler[b], Harold Selnick[a], Zhizhen Zeng[b], Patricia Miller[b], Idriss Bennacef[b], Cristian Salinas[b], Brett Connolly[b], Liza Gantert[b], Marie Holahan[b], Stacey O'Malley[b], Mona Purcell[b], Kerry Riffel[b], Jing Li[c], Jaume Balsells[c], Julie A. OBrien[d], Stacey Melquist[d], Aileen Soriano[e], Xiaoping Zhang[e], Aimie Ogawa[e], Serena Xu[e], Elizabeth Joshi[f], Joseph Della Rocca[g], Fred J. Hess[h], Joel Schachter[h], David Hesk[i], David Schenk[i], Arie Struyk[j], Kerim Babaoglu[k], Talakad G. Lohith[b], Yaode Wang[l], Kun Yang[l], Jianmin Fu[l], Jeffrey L. Evelhoch[b], Paul J. Coleman[a].

[a]Discovery Chemistry, Merck & Co., Inc, West Point PA, USA; [b]Imaging, Merck & Co., Inc, West Point PA, USA; [c]Process Chemistry, Merck & Co., Inc, West Point PA, USA; [d]Pharmacology, Merck & Co., Inc, West Point NJ, USA; [e]Pharmacology, Merck & Co., Inc, Kenilworth NJ, USA; [f]Drug Metabolism, Merck & Co., Inc, West Point PA, USA; [g]Discovery Pharmaceutical Sciences, Merck & Co., Inc, West Point PA, USA; [h]Neuroscience, Merck & Co., Inc, West Point PA, USA; [i]Labelled Compound Synthesis, Merck & Co., Inc, West Point PA, USA; [j]Clinical Pharmacology, Merck & Co., Inc, West Point PA, USA; [k]Computational Chemistry, Merck & Co., Inc, West Point PA, USA; [l]Pharmaron Beijing Co., Ltd, Beijing 100176, China;

1
2
3
4
5
6
7
8
9
10
11
12
13
14
15
16
17
18
19
20
21
22
23
24
25
26
27
28
29
30
31
32
33
34
35
36
37
38
39
40
41
42
43
44
45
46
47
48
49
50
51
52
53
54
55
56
57
58
59
60

ABSTRACT

Neurofibrillary tangles (NFTs) made up of aggregated tau protein have been identified as the pathologic hallmark of several neurodegenerative diseases including Alzheimer's disease. In vivo detection of NFTs using PET imaging represents a unique opportunity to develop a pharmacodynamic tool to accelerate discovery of new disease modifying therapeutics targeting tau pathology. Herein we present the discovery of 6-(fluoro-^{18}F)-3-(1H-pyrrolo[2,3-c]pyridin-1-yl)isoquinolin-5-amine, **6** ([^{18}F]-MK-6240), as a novel PET tracer for detecting NFTs. **6** exhibits high specificity and selectivity for binding to NFTs, with suitable physicochemical properties and in vivo pharmacokinetics.

INTRODUCTION

The search for disease relevant biomarkers for neurodegenerative diseases such as Alzheimer's disease (AD), has received substantial attention within the scientific community over the past decade.[1-5] The main focus in recent clinical trials has been to use cognitive endpoints to measure the effect of therapeutic agents. This requires studying a large number of subjects over long time periods to detect robust changes in these standardized tests and has resulted in an unsustainable financial burden for evaluation of novel disease modifying therapeutics with limited benefits to patients. Therefore, there is an unmet need for sensitive biomarkers that quantify early pathological changes and correlate closely to clinical phenotypes.[1] To satisfy the key criteria for disease relevance the biomarker must be extant at early stages and importantly, show good correlation with the progression of symptoms and signs of the disease.[4] Once validated, clinical applications of the biomarker would go beyond patient selection since

2

measuring pathological changes would provide definitive evidence of therapeutic responses and more confidence for acceleration into larger patient populations.

Within the field of AD-relevant pharmacodynamic biomarkers, earlier research efforts were directed towards measuring human β-amyloid deposition in vivo, which culminated in the discoveries of several β-amyloid positron emission tomography (PET) imaging agents.[6-14] Based on this work β-amyloid PET imaging is recognized as a viable imaging platform for the detection of β-amyloid pathology.[11] However, the recognition that deposited β-amyloid does not correlate to disease progression has rekindled the search for a more relevant biomarker.[15] In contrast to amyloid plaques, neurofibrillary tangles (NFTs) comprised of aggregated tau proteins have shown to better correlate with cognitive decline based on evaluation of Alzheimer's disease autopsy cases.[16-20] Importantly, the density and spread of NFTs within different brain regions has been successfully used to stage disease severity with higher consistency.[21-23] These data strongly supports the quantification of tau pathology as a disease relevant biomarker for in-life diagnosis of AD, more appropriate staging of disease states, and measuring the effect of disease-modifying therapeutics targeting tau pathology.

More recent research efforts have been directed towards extending the success of PET imaging for the in vivo quantification of NFTs.[24-30] The challenges of discovering PET imaging agents for NFTs have been recognized and are subjects of recent reviews.[24, 26, 28] Several discovery efforts have translated into the selection of novel small molecule clinical candidates with high binding affinity to NFTs and selectivity over β-amyloid. From these efforts **1** ([^{18}F]-AV-1451[31-34] a.k.a. [^{18}F]-T807[33, 34]) and **2** ([^{18}F]-T808)[35] were identified as promising early agents, and were followed by the discoveries of **3** ([^{18}F]-THK-5117),[36-38] **4** ([^{18}F]-THK-5351),[39]

5 ([^{11}C]-PBB3),[40, 41] which have been evaluated in early clinical studies (Scheme 1). Currently, **1** has been most extensively studied in AD patients. Although **1** shows excellent selectivity over β-amyloid and has the requisite properties for optimal cell permeability and brain penetration, the signal to background ratio in early AD patients may be smaller than desired.[33] Furthermore, recent reports have suggested **1** shows widespread, high-affinity off-target binding.[42-44] We believe this will have a significant impact on accurately measuring NFT burden in early disease states and confound interpretation of changes in the longitudinal quantification of NFTs. These limitations are attributed to sub-optimal affinity for NFTs and lower selectivity over other brain targets, both of which can be addressed with further optimization of the imaging agent.

Development of an optimal NFT PET tracer as a pharmacodynamic tool for preclinical and clincial research represents a strategic advantage in the development of disease-modifying therapeutics targeting tau pathology. With the objective of identifying a more sensitive and selective NFT PET tracer we initiated an internal PET tracer discovery program. Herein, we describe our research efforts that culminated in the discovery of **6**, an optimized PET imaging agent exhibiting superior in vitro characteristics for NFT binding and clean off-target profile with suitable physicochemical properties and pharmacokinetics in rhesus monkeys.
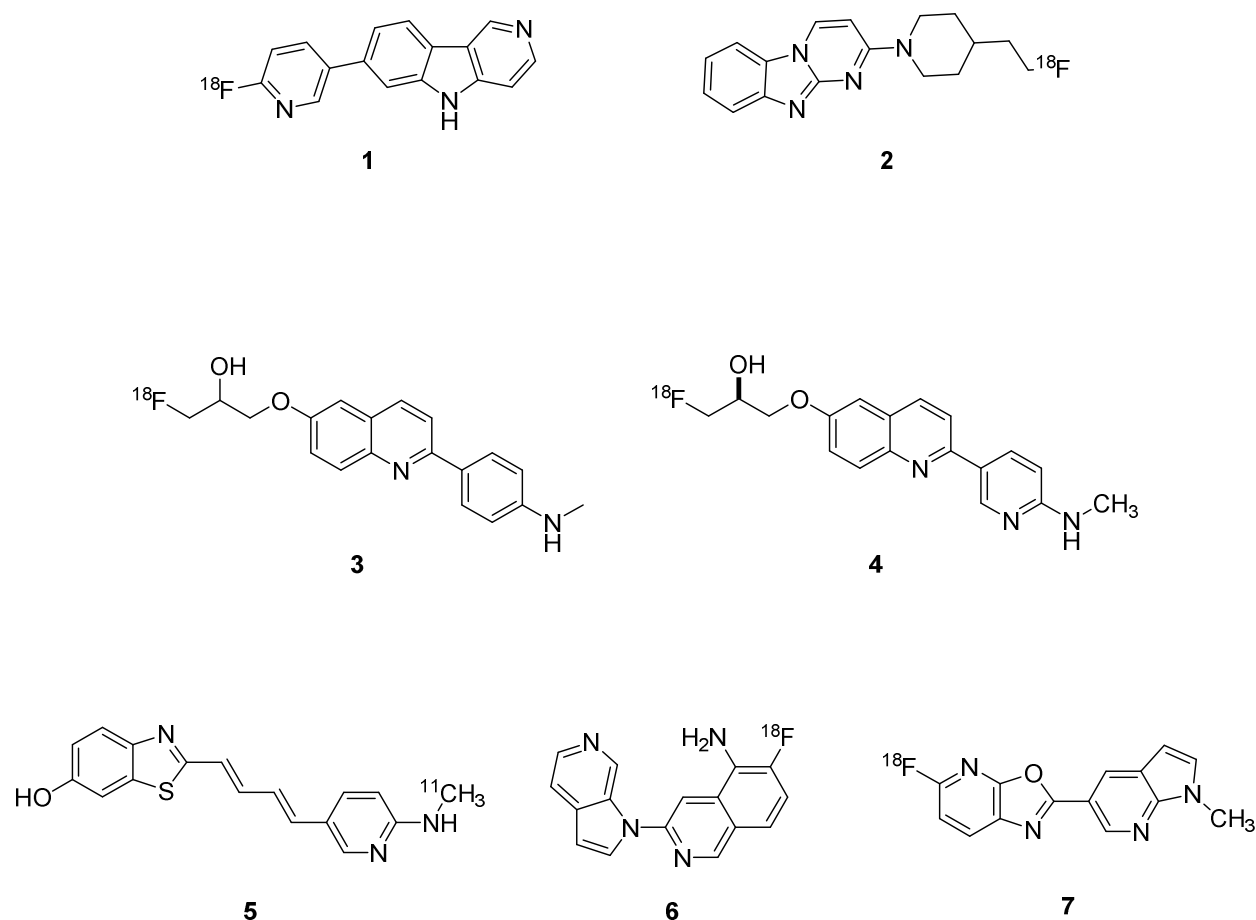
Scheme 1. Chemical structures of NFT PET tracers: **1**, **2**, **3**, **4**, **5**, **6** and β-amyloid PET tracer **7**.

RESULTS and DISCUSSION

The key elements for the identification of an NFT PET tracer were based on achieving high affinity for NFTs and exquisite levels of selectivity over binding to β-amyloid. These were driven by iterative design cycles to establish the SAR with a strong emphasis on improving physicochemical properties to reduce non-specific binding.[45] This was achieved using predictive tools such as lipophilic ligand efficiency (LLE) and measuring the lipophilicity using the shake flask method (sfLogD).[46, 47] To further prioritize compound selection for optimal brain penetration we used Pfizer's CNS-MPO tool and measured P-gp efflux and permeability.[48]

Central to the routine clinical application of a PET tracer for NFTs is the limitation around the use of an [^{11}C] tracer due to the short half-life (~20 min) of carbon-11 requiring an on-site cyclotron. Therefore, the chemistry strategy focused on establishing the molecular connectivity, starting from the minimal pharmacophore, which allowed the incorporation of the ^{18}F isotope without compromising the desired properties. Finally, the PET candidate needed to demonstrate no white matter binding in nonhuman primates and no evidence of brain-penetrant metabolites.

Our discovery efforts began with assessing the most suitable screening strategy to identify novel chemical matter for lead optimization. First we initiated a competitive binding assay in in vitro assembled tau filaments using radiolabeled Thioflavin T as the reference radioligand. However, we quickly recognized a similar discrepancy to that reported by Kolb and coworkers,[34] in correlating the observed binding affinity to human AD brain tissue. Based on this data and our previous experience in the discovery of **7** ([^{18}F]-MK-3328),[14, 49] a novel β-amyloid PET ligand, we developed a complimentary competition binding assay for NFTs in human AD cortex homogenates to characterize newly designed compounds. Although the tau filament based assay could not be used directly to drive our discovery efforts, we were able to screen the Merck compound collection and prioritized a novel scaffold for identification of a new reference radioligand and lead optimization using the AD cortical homogenate assays.

From our lead identification efforts we selected aza-indole **8**, which was synthesized using copper catalyzed C-N bond formation from commercially available starting materials (**8a** & **8b**) (Scheme 1). After rhodium mediated tritium labelling, [^{3}H]**8** was evaluated as a radioligand in human AD brain homogenates.[50] [^{3}H]**8** has a K_d of 0.3 nM for binding to NFTs in human AD brain homogenates with low levels of nonspecific binding, making it a highly suitable radioligand for competition binding assays. Furthermore, it exhibited high selectivity (Ki >10

µM) for binding to β-amyloid using **[³H]7** as the reference radioligand in human AD brain homogenates. Based on the in vitro specificity, selectivity, and the excellent physicochemical properties we dedicated further efforts to investigate this series.
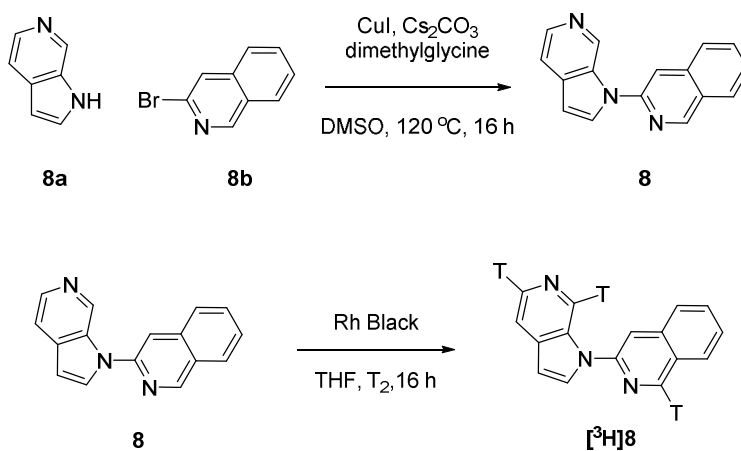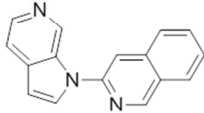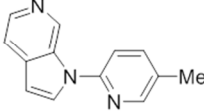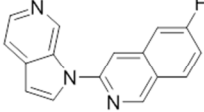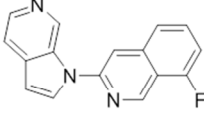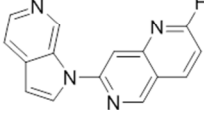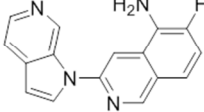
Scheme 2. Chemical synthesis of **8** and [³H]**8**.

A thorough SAR analysis of the structural elements revealed that the aza-indole core with a 2,4-substituted pyridine, represented by compound **9** (K_i = 8.8 nM) (Scheme 3), was the minimal pharmacophore required for high binding affinity to NFTs within this series. Unfortunately, introduction of fluorine atoms within this minimal pharmacophore on positions enabled for direct radiochemical introduction of fluorine-18 resulted in a >10 fold loss in affinity (Scheme 3). This was the case when either heterocyclic ring was fluorinated, suggesting a specific electronic contribution to NFT binding from the basic nitrogen atoms. Therefore we shifted our lead optimization efforts to compound **8** and functionalized the isoquinoline with fluorine atoms on the 6 and 8 position (compound **10** & **11**), which are also activated for nucleophilic aromatic substitution (S$_N$Ar).
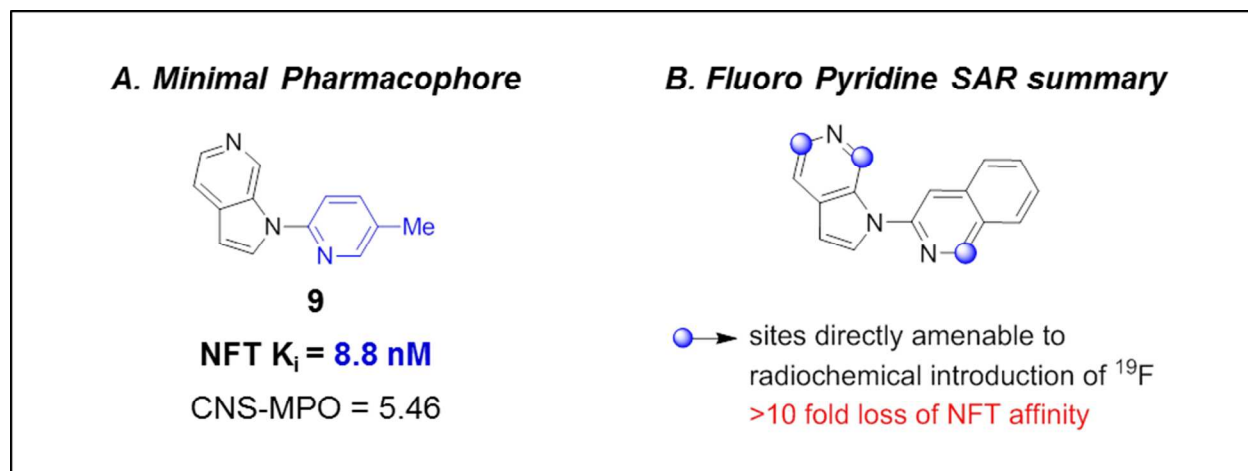
Scheme 3. (A) Identification of minimal pharmacophore for NFT affinity. **(B)** SAR exploration of fluorinated analogs of compound **8**.

Chemical syntheses of compound **10** & **11** (Schemes 4 & 5) were initiated from the appropriately substituted indanones which were reacted with isoamylnitrite to form 2-(oximino)indan-1-ones **10b** & **11b**. Ring expansion to the 1,3-dichloroisoquinolines was achieved after reaction with PCl_5 in $POCl_3$ followed by treatment with anhydrous HCl. Regioselective reduction of the chlorine atom in the 3 position with red phosphorous provided the key coupling partners for palladium catalyzed C-N bond formation to give the final products **10** & **11**. Both fluorinated isoquinoline isomers exhibited similar high affinity binding to NFTs using [^{3}H]**7**, and high selectivity to β-amyloid using [^{3}H]**7** in competition binding assays using human AD brain homogenates (Table 1). Compound **10** was prioritized for further in vitro and in vivo studies based on higher affinity for NFTs than **10** and more robust radiochemistry starting from the corresponding 6-substituted nitro precursor (Scheme 6) to yield [^{18}F]**10**. [^{3}H]**10** was also prepared directly from **10** using the direct tritiation method.[50]

Compound		CNS-MPO	sfLogD	NFT [³H]8 K_i (nM)	β-amyloid [³H]7 K_i (nM)
8		5.06	2.43	0.30	>10000
9		5.46	nd	8.8	>10000
10		5.0	3.6	0.22	>10000
11		5.0	nd	0.91	>10000
12		6.0	2.90	52.6	>10000
6		5.82	3.32	0.36	>10000

Table 1. Physicochemical properties, NFT binding affinity and β-amyloid selectivity of selected compounds **1-6**. (nd = not detemined)
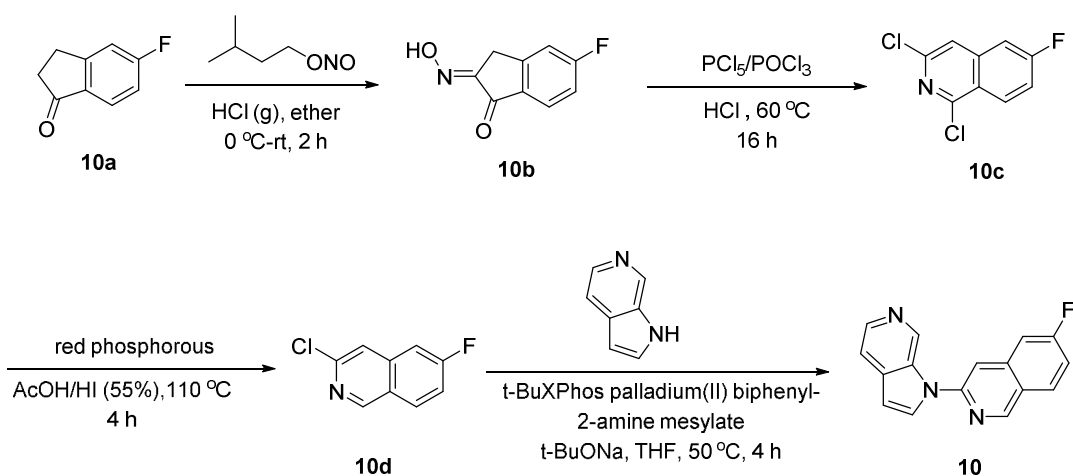
Scheme 4: Chemical Synthesis of compound **10**
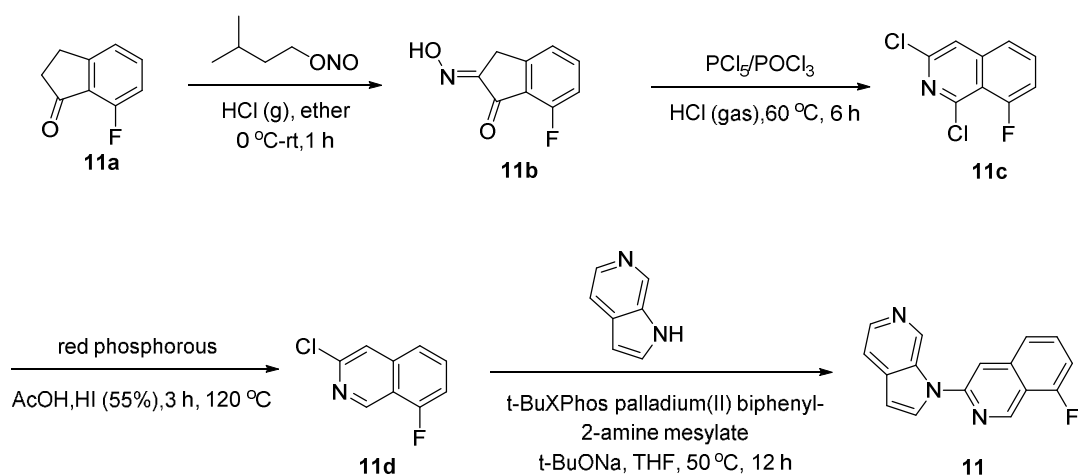
Scheme 5: Chemical Synthesis of compound **11**
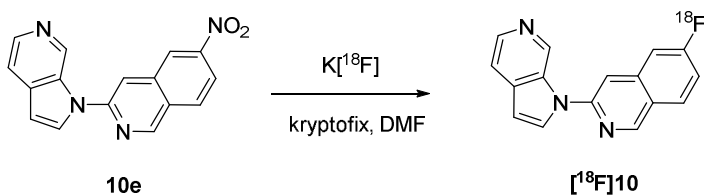
Scheme 6: Radiochemical Synthesis of compound [^{18}F]**10**

In NFT-rich AD brain tissue homogenates, saturation binding studies show [^{3}H]**10** has a high affinity for NFTs (K_d = 1.2 nM) (Table 2) which translates to a large predicted in vivo signal based on the high B_{max} / K_d ratio (~121).[51] However, the lipophilicity of compound **10** was higher than desired as measured using the shake flask method (sfLogD = 3.6). To further investigate the potential impact of the high lipophilicity we performed in vivo studies in rhesus monkeys. Although these monkeys do not exhibit tau pathology, the PET studies were designed to inform on the intrinsic physicochemical and pharmacokinetic properties of the molecule. [^{18}F]**10** distributes rapidly across the blood-brain barrier (BBB) followed by rapid clearance (Figure 2, panel A). However, the distribution is not homogeneous across all brain regions with significant retention in white matter (Figure 2, panels A and C). This data was very informative as it unveiled a significant liability which would reduce the in vivo sensitivity of compound **10**, due to higher background signal directly attributed to suboptimal physicochemical properties.

With the goal of reducing non-specific binding of compound **10**, we designed several modifications aimed at modulating the polar surface area to decrease overall lipophilicity. Based on predicted properties the most promising modifications included: (a) addition of a nitrogen within the isoquinoline converting to a naphthyridine ring (compound **12**) and (b) introduction of an amine on the isoquinoline ring system (compound **6**). Compound **12** was prepared in 7 steps (Scheme 7) starting from direct nucleophilic aromatic substitution of aza-indole **8a** with methyl 5-bromo-2-chloroisonicotinate **12a** under basic conditions to give the hydrolyzed isonicotinic acid **12b**. The carboxylic acid was subjected to Curtius rearrangement in the presence of *t*-BuOH and deprotected to give the tri-substituted pyridine **12d**. Heck coupling with ethyl acrylate followed by intramolecular lactamization and phosphorus oxychloride mediated chlorination gave the chlorinated napthyridine **12g**. Introduction of flouride was achieved under

standard conditions using potassium flouride to give fluoro-naphthyridine **12**. Synthesis of

compound **6** (Scheme 8) was initiated from direct nitration of previously synthesized

isoquoniline **10d**. Reduction of the nitro group using iron in acetic acid followed by protection

of the aniline nitrogen gave the key substrate (**6d**) for coupling with aza-indole **8a**. Palladium

catalyzed C-N bond formation with *t*-BuXPhos followed by deprotection with trifluoroacetic

acid gave the fluoro-aniline **6**.
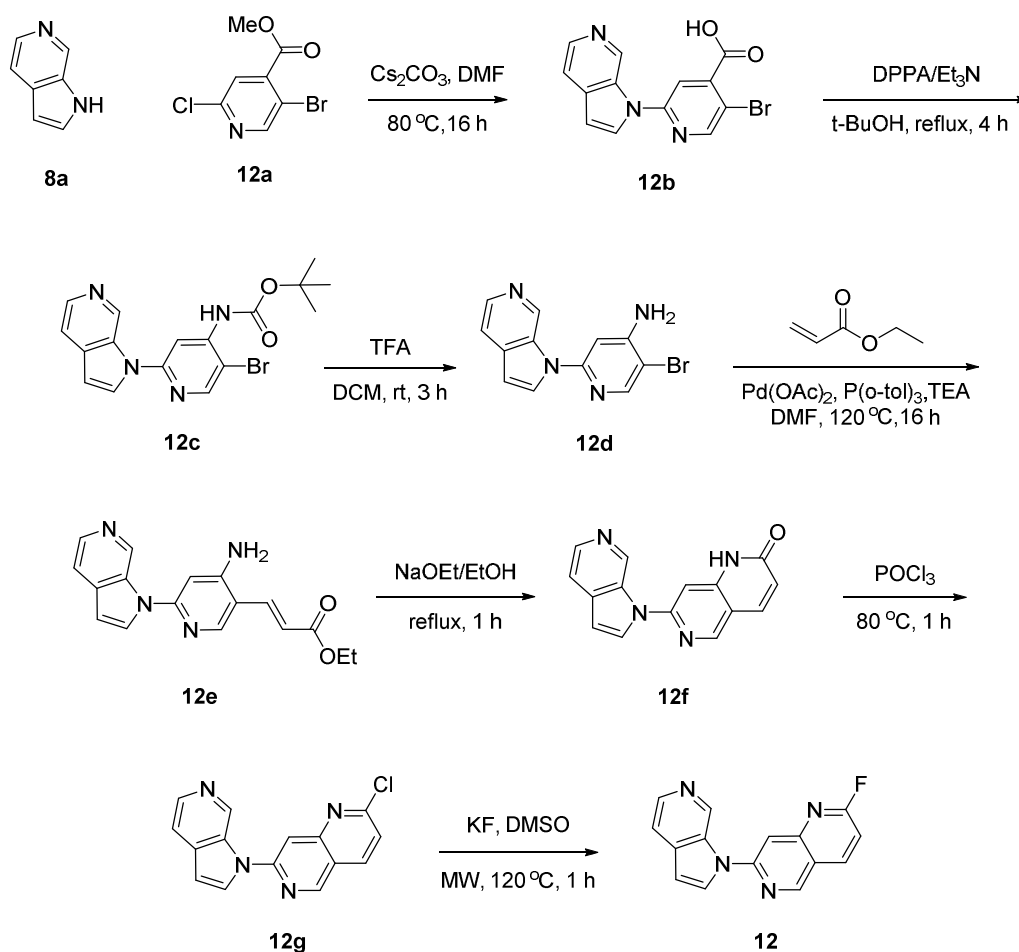
Scheme 7: Chemical synthesis of compound **12**.
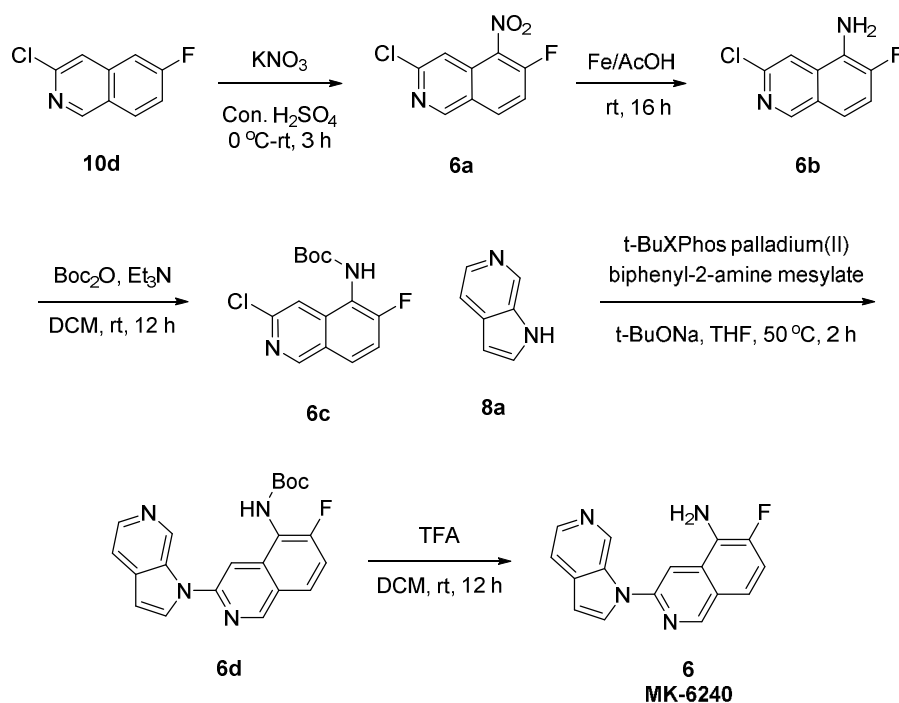
Scheme 8: Chemical synthesis of compound **6**.

The strategic introduction of nitrogen atoms resulted in reduction of lipophilicity and predicted overall improvement in the physicochemical properties for both compounds **5** & **6**, as calculated using the CNS-MPO (>5.5) scores and measured shake flask log D (2.9-3.3) (Table 1). Fluoro-naphthyridine **5** presented the potential for improved ^{18}F-radiochemistry via direct nucleophilic displacement starting from the activated 2-nitro-naphthyridine. However, the fluoro-naphthyridine **5** exhibited a significant loss in affinity for binding to NFT compared to the fluoro-isoquinoline **3** (>200 fold loss in NFT affinity, Table 1). Interestingly, fluoro-aniline **6** maintained a similar in vitro profile to **3** in competition binding assays with [^{3}H]**1** for binding to NFT and against [^{3}H]-**7** for selectivity against β-amyloid. Compound **6** was not a substrate for human or rat P-glycoprotein (P-gp) mediated efflux (BA:AB ~1.3 @ 0.1 μM) in the P-gp expressing LLC-PK1 cell line, and showed high passive permeability in control LLC-PK1 cells

(Papp > 29 x 10^{-6} cm•s^{-1}). Evaluation of **6** in a counter-screen panel of 118 receptor and enzyme targets revealed no ancillary activities with IC_{50} values > 1 µM. Based on this data tritium labeled [^{3}H]**6** was prepared for further characterization in in vitro studies.

Evaluation of [^{3}H]**6** in saturation binding studies in NFT-rich AD cortex homogenates confirmed the high affinity saturable binding to NFTs (K_d = 0.42 nM) with consistent high B_{max} / K_d ratio (~211) to that observed in studies with [^{3}H]**10** (Table 2). To evaluate the selectivity of **6** for binding to NFTs, we used **2** as the blocking agent to represent a structurally distinct and selective NFT ligand. We observed a similar B_{max} / K_d ratio (~238) to that obtained with self-block (Table 2), suggesting minimal to no off-target binding. A lack of binding was also confirmed in non-AD cortex homogenates under similar conditions (data not shown). A comparative study using **2** to define non-displaceable binding, revealed that compound [^{3}H]**6** had at least 2 fold higher B_{max} / K_d ratio compared to [^{3}H]**1**. The higher B_{max} / K_d ratio suggests higher sensitivity for compound **6** for binding to NFTs which is proportional to the in vivo signal from a PET imaging agent.[51] Autoradiographic imaging studies with human AD brain slices were used to qualitatively validate the binding characteristics of **6**. [^{3}H]**6** showed a strong signal with high amount of displaceable binding in the grey matter (region of high NFT load) by either self-block (Figure 1B) or block with **2** (Figure 1C), and the observed binding pattern matched closely with immunostaining for NFTs using PHF6 (Figure 1D). Based on this data compound **6** exhibited superior in vitro specificity and selectivity characteristics, and was prioritized for further studies in vivo.

	AD Cortex [³H]10 block 1μM (10)	AD Cortex [³H]10 block 50nM (8)	AD Cortex [³H]6 block 100xK$_d$ (6)	AD Cortex [³H]6 block 100xK$_d$ (2)	AD Cortex [³H]1 block 100xK$_d$ (2)
NFT-rich AD K_d	1.2 nM	0.8 nM	0.42 nM	0.34 nM	1.1 nM
NFT-rich AD B_{max}	145 nM	104 nM	88.5 nM	80.8 nM	119.6 nM
NFT-rich AD B_{max}/K_d	121	130	211	238	109

Table 2. B_{max} and K_d values for [³H]**10**, [³H]**6** and [³H]**1** binding in NFT-rich AD brain tissues. Data are determined using same pool of brain homogenates.
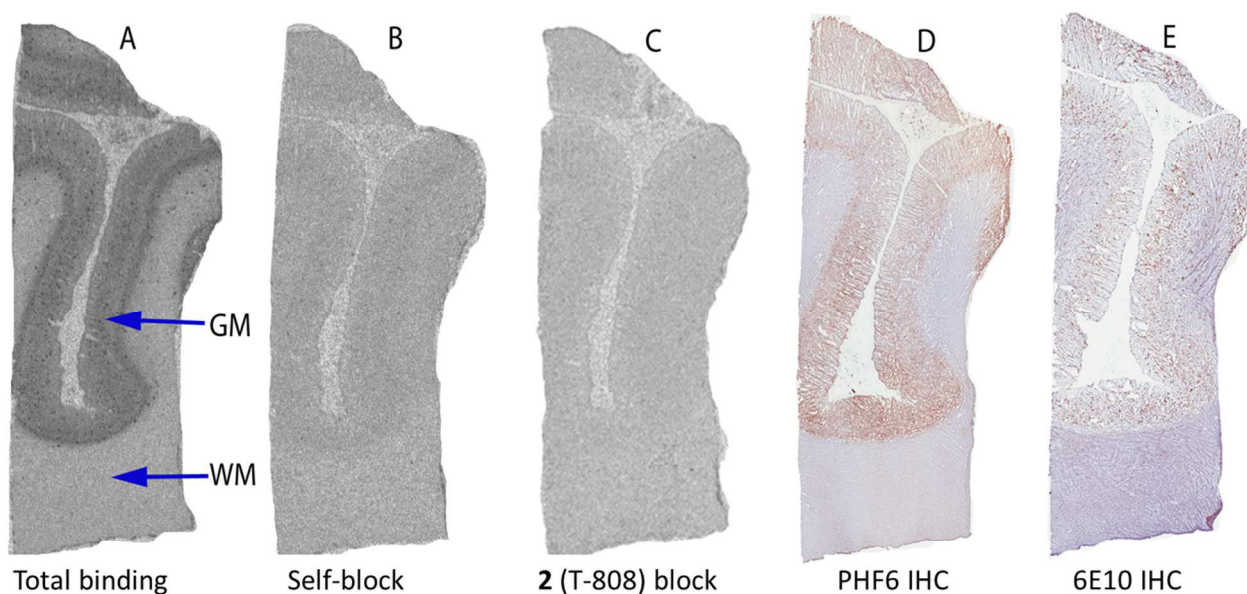
Figure 1(A-E). Results from autoradiography studies with [³H]**6** and immunohistochemistry in the frontal cortex (FC) of an NFT-rich AD brain donor. **A.** [³H]**6** total binding GM/WM ratio = 5.4; **B.** [³H]**6** + 50 nM (**6**) GM/WM ratio = 1.2; **C.** [³H]**6** + 500 nM **2** GM/WM ratio = 1.1; **D.** PHF6 staining for phospho-tau. **E.** 6E10 IHC staining for amyloid; GM = grey matter, WM = white matter;

To enable in vivo evaluation of its physicochemical and pharmacokinetic properties in rhesus monkey PET studies, [¹⁸F]**6** was synthesized from the 5-diBoc-6-nitro precursor **6e** in 2 synthetic steps (Scheme 9). Baseline PET studies showed [¹⁸F]**6** has favorable pharmacokinetic

properties, with high distribution into the brain followed by rapid clearance (Figure 2, panel B).

Gratifyingly, the effect of improved physicochemical properties was also evident in vivo as no

white matter retention was observed with homogenous distribution across all brain regions since

rhesus monkey do not exhibit tau pathology (Figure 2, panel D). In vitro metabolism studies in

monkey liver microsomes predicted low levels of oxidative defluorination which manifested as

minimal skull uptake in vivo. In contrast, similar studies in human liver microsomes showed

lower levels of oxidative defluorination (data not shown). To ensure minimal impact on

quantifying changes in NFT signal the extent of defluorination will need to be monitored in early

clinical validation studies.
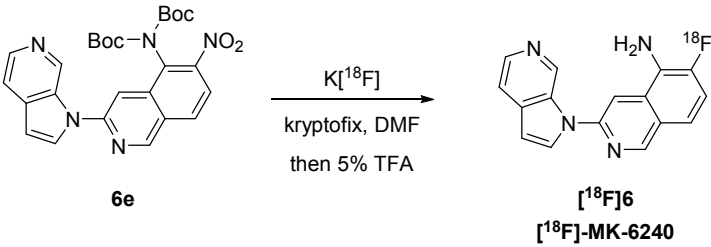
Scheme 9: Radiochemical Synthesis of compound [^{18}F]**6**
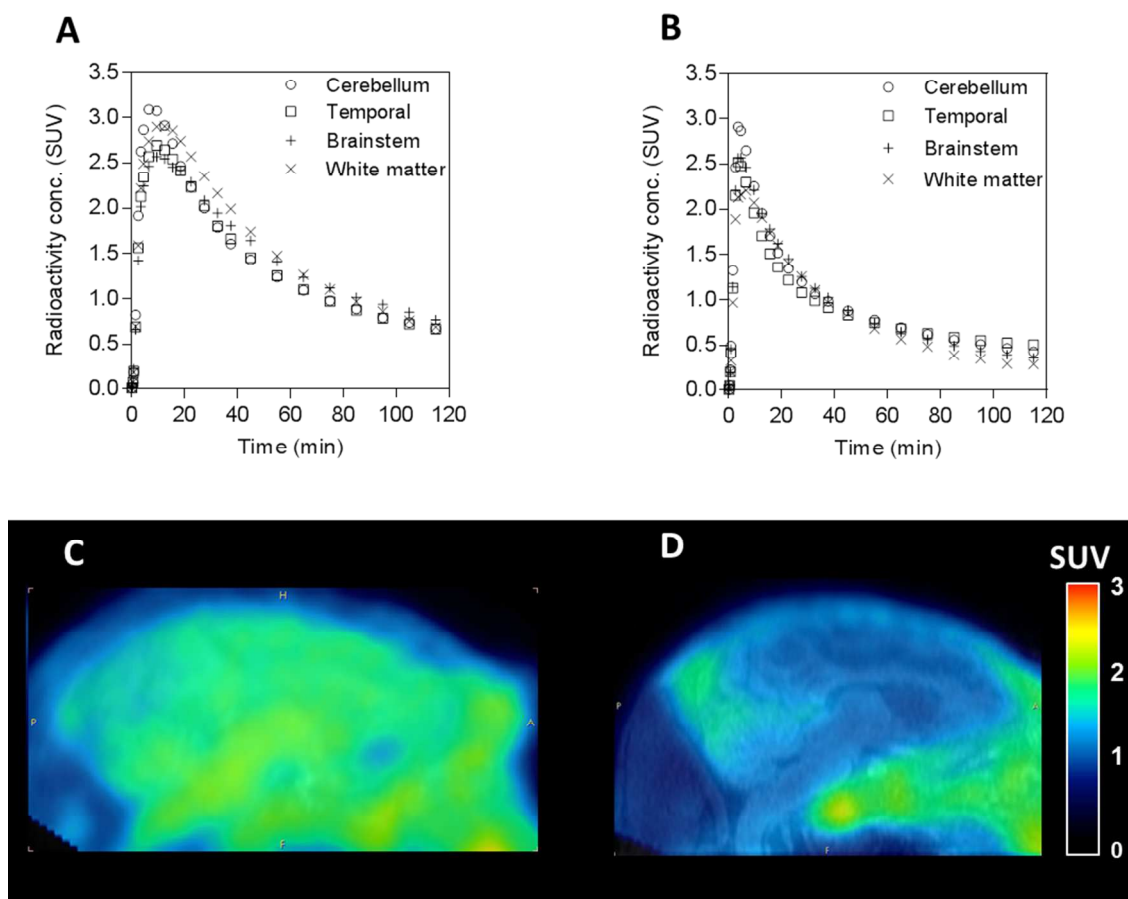
Figure 2: Regional time-activity curves and summed PET image (40-80 min) from a rhesus monkey overlaid on an MR image in saggital plane. Panels A and C are from [^{18}F]**10** and panels B and D are from [^{18}F]**6**. Radioactivity concentration is expressed as standardized uptake value (SUV) that is normalized to injected dose and body weight.

To further evaluate the imaging characteristics of [^{18}F]**6** we designed an in vivo PET blocking study in rhesus monkey. In this experiment a high dose of **6** was administered prior to tracer level dosage of [^{18}F]**6**, and the resulting PET data was compared to a baseline PET study with [^{18}F]**6**. As shown in figure 3, the level of tracer retention did not change between the baseline and self-block studies, indicating **6** has no high affinity off-target binding to CNS targets that could interfere with detection NFTs in human. Based on these favorable preclinical

17

1
2
3
4
5
6
7
8
9
10
11
12
13
14
15
16
17
18
19
20
21
22
23
24
25
26
27
28
29
30
31
32
33
34
35
36
37
38
39
40
41
42
43
44
45
46
47
48
49
50
51
52
53
54
55
56
57
58
59
60

data, [^{18}F]**6** was selected to move into early clinical studies and designated as [^{18}F]-MK-6240.

Extensive preclinical in vitro and in vivo studies with **6** have been completed and will be

communicated shortly.   Further exploratory in vitro studies will be required to determine the

utility and binding characteristics of **6** to NFTs in tissue from non-AD tauopathies.
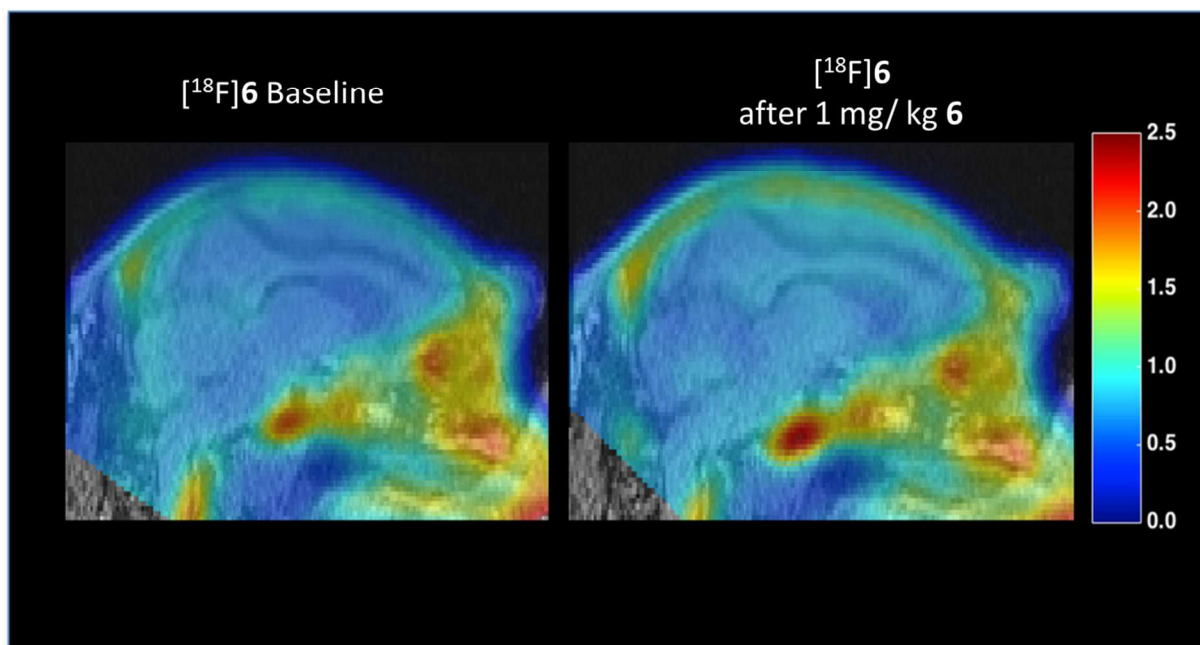
Figure 3. Comparison of summed PET images (90-120 min, sagittal view) overlaid on an MR image from PET studies with [^{18}F]**6** at baseline (left image) and after 1 mpk **6** (right image) in rhesus monkey; scale is in SUV.

CONCLUSIONS

In summary, we have identified a novel imaging agent for detecting tau pathology, **6**, with

exquisite in vitro binding affinity to NFTs, high selectivity to β-amyloid, and excellent

physicochemical properties for brain penetration and cellular permeability.   **6** exhibits no off-

target binding with suitable in vivo pharmacokinetics and merits clinical evaluation as a PET

ligand for the quantification of NFTs in AD patients. Clinical studies to evaluate $[^{18}F]$**6** as an NFT PET tracer in Alzherimer's disease patients are currently underway and will be reported in due course.

EXPERIMENTAL SECTION

General Methods

All solvents used were commercially available "anhydrous" grade, and reagents were used without purification unless otherwise noted. Non-aqueous reactions were carried out in oven- or heatgun- dried glassware under a $N_2(g)$ atmosphere. Magnetic stirring was used to agitate the reactions and they were monitored for completion by either TLC (silica gel 60, Merck) or LC–MS. A Smith Creator microwave from Personal Chemistry was used for microwave heating, and a CombiFlash system using RediSep cartridges by Teledyne Isco was used for silica gel chromatography with fraction collection at 254 nm. Reversed-phase HPLC purification was carried out on a Waters HPLC (XBridge Prep C_{18} 5 μm 19_150 mm column) using a gradient of 0.1% TFA in H_2O/CH_3CN with sample collection triggered by photodiode array detection. The reported yields are for isolated compounds of ≥95% purity which was determined by HPLC and ^{1}H-NMR. HPLC was carried out with a Waters 2690 Separations Module equipped with a YMC Pro 50x3 mm i.d. C18 column interfaced with a Waters Micromass ZMD spectrometer using a gradient of 0.05% TFA in H_2O/CH_3CN with UV detection at 215 and 254 nm. ^{1}H spectra were recorded on a Varian INOVA 400 or 500 MHz spectrometer, and all chemical shifts are referenced to an internal standard of tetramethylsilane or the $CDCl_3$ solvent peak, respectively. All temperatures are degrees Celsius unless otherwise noted. Mass spectra (MS) were measured by electrospray ion-mass spectroscopy (ESI).

Chemical synthesis of final compounds 6, 8, 9, 10, 11, 12:

6-Fluoro-3-(1H-pyrrolo[2,3-c]pyridin-1-yl)isoquinolin-5-amine (6):

Step 1. 3-Chloro-6-fluoro-5-nitroisoquinoline (6a): To a solution of 3-chloro-6-fluoroisoquinoline (**10d**) (2.0 g, 11.0 mmol) in concentrated sulfuric acid (30 mL) was added potassium nitrate (1.2 g, 11.6 mmol) at 0 °C. The resulting mixture was stirred for 3 hours at ambient temperature then poured onto ice/water (200 g). A filtration was performed and the filter cake was washed with water (2 x 10 mL), purified by silica gel column chromatography, eluted with 10~20% ethyl acetate in petroleum ether to afford **6a** as a light-yellow solid (1.0 g, 40%): ^{1}H NMR (300 MHz, DMSO-d_6) δ 9.43 (s, 1H), 8.70-8.65 (m, 1H), 8.07 (s, 1H), 8.00-7.93 (m, 1H); LC/MS: $[(M +1)]^+ = 227.0$.

Step 2. 3-Chloro-6-fluoroisoquinolin-5-amine (6b): To a solution of 3-chloro-6-fluoro-5-nitroisoquinoline (**6a**) (1.0 g, 4.41 mmol) in acetic acid (30 mL) was added iron powder (1.24 g, 22.07 mmol). The resulting mixture was stirred for 16 hours at ambient temperature, then filtered through Celite and the filtrate was concentrated under reduced pressure. The residue was taken up with water (50 mL, saturated with sodium bicarbonate) and the resulting mixture was extracted with ethyl acetate (4 x 100 mL). The combined organic layers was dried over anhydrous sodium sulfate. After filtration, the filtrate was concentrated under reduced pressure and the residue was purified by silica gel column chromatography, eluted with 1% methanol in dichloromethane to afford **6b** as a yellow solid (0.75 g, 86%): ^{1}H NMR (300 MHz, DMSO-d_6) δ 9.06 (s, 1H), 8.26 (s, 1H), 7.51-7.44 (m, 1H), 7.40-7.35 (m, 1H), 6.01 (br s, 2H); LC/MS: $[(M +1)]^+ = 197.1$.

Step 3. tert-Butyl N-[(tert-butoxy)carbonyl]-N-(3-chloro-6-fluoroisoquinolin-5-yl)carbamate (6c): To a solution of 3-chloro-6-fluoroisoquinolin-5-amine (0.35 g, 1.78 mmol) in dichloromethane (60 mL) were added di-tert-butyl dicarbonate (0.97 g, 4.45 mmol), triethylamine (0.36 g, 3.56 mmol) and *N,N*-dimethylpyridin-4-amine (0.02 g, 0.18 mmol). The resulting mixture was stirred for 12 hours at ambient temperature. After that, the reaction was quenched with water (100 mL) and extracted with ethyl acetate (3 x 100 mL). The combined organic layers was washed with brine (30 mL) and dried over anhydrous sodium sulfate. After filtration, the filtrate was concentrated under reduced pressure and the residue was purified by silica gel column chromatography, eluted with 1~2% methanol in dichloromethane to afford **6c** as a yellow solid (0.45 g, 62%): ^{1}H NMR (300 MHz, CDCl$_3$) δ 9.07 (s, 1H), 8.01-7.98 (m, 1H), 7.67 (s, 1H), 7.45-7.40 (m, 1H), 1.37 (s, 18H); LC/MS: $[(M +1)]^+ = 197.0$.

Step 4. tert-Butyl 6-fluoro-3-(1H-pyrrolo[2,3-c]pyridin-1-yl)isoquinolin-5-ylcarbamate (6d): To a solution of 1H-pyrrolo[2,3-c]pyridine (**8a**) (0.20 g, 1.70 mmol) in tetrahydrofuran (80 mL) were added tert-butyl N-[(tert-butoxy)carbonyl]-N-(3-chloro-6-fluoroisoquinolin-5-yl)carbamate (**6c**) (0.45 g, 1.13 mmol), sodium 2-methylpropan-2-olate (0.22 g, 2.27 mmol) and t-BuXPhos Palladium (II) biphenyl-2-amine mesylate (0.09 g, 0.11 mmol) at ambient temperature. The resulting mixture was stirred for 2 hours at 50 °C under nitrogen atmosphere. After cooling down to ambient temperature, the resulting mixture was diluted with water (100 mL) and extracted with ethyl acetate (3 x 100 mL). The combined organic layers was washed with brine (100 mL) and dried over anhydrous sodium sulfate. After filtration, the filtrate was concentrated under reduced pressure and the residue was purified by silica gel column chromatography, eluted with 1~2% methanol in dichloromethane to afford **6d** as a yellow solid (0.35 g, 79%): ^{1}H NMR (300 MHz, CDCl$_3$) δ 9.68 (s, 1H), 9.22 (s, 1H), 8.37 (d, *J* = 4.8 Hz, 1H),

8.07 (d, J = 3.3 Hz, 1H), 7.99-7.93 (m, 2H), 7.63 (d, J = 5.7 Hz, 1H), 7.44-7.26 (m, 1H), 6.80 (d, J = 3.3 Hz, 1H), 6.50 (br s, 1H), 1.56 (s, 9H); LC/MS: $[(M +1)]^+$ = 379.2.

Step 5. 6-Fluoro-3-(1H-pyrrolo[2,3-c]pyridin-1-yl)isoquinolin-5-amine (6): A solution of tert-butyl 6-fluoro-3-(1H-pyrrolo[2,3-c]pyridin-1-yl)isoquinolin-5-ylcarbamate (**6d**) (0.35 g, 0.93 mmol) in dichloromethane (50 mL) was treated with trifluoroacetic acid (3.16 g, 27.70 mmol) for 12 hours at ambient temperature. The resulting mixture was concentrated under reduced pressure and the residue was dissolved into dichloromethane (50 mL), washed with saturated aqueous solution of sodium bicarbonate (50 mL). The organic layer was dried over anhydrous sodium sulfate. After filtration, the filtrate was concentrated under reduced pressure and the residue was purified by silica gel column chromatography, eluted with 1-2% methanol in dichloromethane to afford **6** as a yellow solid (0.24 g, 90%): ^{1}H NMR (300 MHz, DMSO-d_6) δ 9.70 (s, 1H), 9.27 (s, 1H), 8.40 (s, 1H), 8.35-8.27 (m, 2H), 7.68-7.66 (m, 1H), 7.45-7.43 (m, 2H), 6.88 (d, J = 3.3 Hz, 1H), 6.03 (br s, 2H); LC/MS: $[(M +1)]^+$ = 279.1.

3-(1H-Pyrrolo[2,3-c]pyridin-1-yl)isoquinoline (8): To a stirred solution of 1H-pyrrolo[2,3-c]pyridine (**8a**) (0.20 g, 1.69 mmol) in dimethyl sulfoxide (30 mL) were added 3-bromoisoquinoline (**8b**) (0.38 g, 1.86 mmol), dimethylglycine (0.07 g, 0.68 mmol), cesium carbonate (2.20 g, 6.77 mmol) and copper (I) iodide (0.19 g, 1.01 mmol). The resulting mixture was stirred for 16 hours at 120 °C under a nitrogen atmosphere. After cooling down to ambient temperature, the reaction was quenched by water (200 mL) and extracted with ethyl acetate (3 x 50 mL). The combined organic layers was washed with brine (3 x 100 mL), dried over anhydrous sodium sulfate and filtered. The filtration was concentrated under reduced pressure and the residue was purified by silica gel column chromatography, eluted with 1~1.5% methanol in dichloromethane to afford **8** as a brown solid (0.38 g, 92%): ^{1}H NMR (400 MHz, DMSO-d_6)

δ 9.69 (br s, 1H), 9.42 (s, 1H), 8.35 (d, *J* = 3.2 Hz, 1H), 8.27 (s, 2 H), 8.20 (d, *J* = 8.4 Hz, 1H), 8.06 (d, *J* = 8.0 Hz, 1H), 7.84 (t, *J* = 8.0 Hz, 1H), 7.68-7.65 (m, 2H), 6.87 (d, *J* = 3.6 Hz, 1H); LC/MS: $[(M +1)]^+$ = 246.1.

1-(5-Methylpyridin-2-yl)-1H-pyrrolo[2,3-c]pyridine (9): To a stirred solution of 1H-pyrrolo[2,3-c]pyridine (**8a**) (0.10 g, 0.84 mmol) in dimethyl sulfoxide (20 mL) were added 2-bromo-5-methylpyridine (**9a**) (0.19 g, 1.10 mmol), dimethylglycine (0.035 g, 0.34 mmol), cesium carbonate (1.10 g, 3.39 mmol) and copper (I) iodide (0.097 g, 0.51 mmol). The resulting mixture was stirred for 16 hours at 120 °C under a nitrogen atmosphere. After cooling down to ambient temperature, the reaction was quenched by water (30 mL) and extracted with ethyl acetate (3 x 30 mL). The combined organic layers was washed with brine (100 mL), dried over anhydrous sodium sulfate and filtered. The filtration was concentrated under reduced pressure and the residue was purified by silica gel column chromatography, eluted with 1~4% methanol in dichloromethane to afford **9** as a light yellow solid (51 mg, 29%): ^{1}H NMR (300 MHz, DMSO-*d₆*) δ 9.68 (s, 1H), 8.54 (s, 1H), 8.27-8.26 (m, 2H), 7.85 (d, *J* = 8.7 Hz, 1H), 7.77 (d, *J* = 8.4 Hz, 1H), 7.64 (d, *J* = 5.1 Hz, 1H), 6.81 (d, *J* = 3.0 Hz, 1H), 2.36 (s, 3H); LC/MS: $[(M +1)]^+$ = 210.1.

6-Fluoro-3-(1H-pyrrolo[2,3-c]pyridin-1-yl)isoquinoline (10):

Step 1. (*E*)-5-fluoro-2-(hydroxyimino)-2,3-dihydroinden-1-one (10b):   To a stirred solution of 5-fluoro-2,3-dihydroinden-1-one (**10a**) (22 g, 147 mmol) in diethyl ether (500 mL) was added a saturated solution of dry hydrochloride gas in methanol (22 mL) followed by the addition of isopentyl nitrite (26 g, 220 mmol) at 0 °C. After stirred for 2 hours at ambient temperature, solids were collected by filtration and washed with diethyl ether (200 mL) to afford

10b as a yellow solid (21 g, 79%): ^{1}H NMR (400 MHz, DMSO-d_6) δ 12.67 (s, 1H), 7.85-7.81 (m, 1H), 7.46-7.43 (m, 1H), 7.31-7.28 (m, 1H), 3.79 (s, 2H); LC/MS: $[(M +1)]^+$ = 180.0.

Step 2. 1,3-Dichloro-6-fluoroisoquinoline (10c): To a stirred solution of (E)-5-fluoro-2-(hydroxyimino)-2,3-dihydroinden-1-one (**10b**) (25 g, 140 mmol) in phosphorus oxytrichloride (400 mL, saturated with hydrochloride) was added pentachlorophosphorane (73 g, 349 mmol). The resulting mixture was stirred for 16 hours at 60 °C. After cooling down to ambient temperature, the resulting mixture was concentrated under reduced pressure and the residue was triturated with water (500 mL) and filtered. The filter cake was washed with water (200 mL) and dried in a vacuum oven to afford **10c** as a yellow solid (28 g, 93%): ^{1}H NMR (400 MHz, CDCl$_3$) δ 8.42-8.35 (m, 1H), 7.68 (s, 1H), 7.47-7.41 (m, 2H); LC/MS: $[(M +1)]^+$ = 216.0.

Step 3. 3-Chloro-6-fluoroisoquinoline (10d): To a stirred solution of 1,3-dichloro-6-fluoroisoquinoline (**10c**) (28 g, 130 mmol) in acetic acid (500 mL) and hydriodic acid (250 mL, 55% w/w aqueous solution) was added red phosphorus (10 g, 324 mmol) at ambient temperature. The resulting mixture was stirred for 4 hours at 110 °C. After cooling down to ambient temperature, the resulting mixture was concentrated under reduced pressure. The residue was taken up by ethyl acetate (500 mL) and water (500 mL). The organic layer was separated out and the aqueous layer was extracted with ethyl acetate (2 x 500 mL). The combined organic layers was washed with brine (300 mL) and dried over anhydrous sodium sulfate. After filtration, the filtrate was concentrated under reduced pressure and the residue was purified by silica gel column chromatography, eluted with 0~10% ethyl acetate in petroleum ether to afford **10d** as a yellow solid (20 g, 85%): ^{1}H NMR (300 MHz, CDCl$_3$) δ 9.04 (s, 1H), 8.06-7.97 (m, 1H), 7.68 (s, 1H), 7.39-7.35 (m, 2H); LC/MS: $[(M +1)]^+$ = 182.1.

Step 4. 6-Fluoro-3-(1H-pyrrolo[2,3-c]pyridin-1-yl)isoquinoline (10): To a stirred solution of 1H-pyrrolo[2,3-c]pyridine (**8a**) (1.14 g, 9.66 mmol) and 3-chloro-6-fluoroisoquinoline (**10d**) (1.17 g, 6.44 mmol) in tetrahydrofuran (60 mL) was added sodium 2-methylpropan-2-olate (1.24 g, 12.89 mmol) and t-BuXPhos palladium(II) biphenyl-2-amine mesylate (0.26 g, 0.32 mmol) at ambient temperature. The resulting mixture was stirred for 4 hours at 50 °C under a nitrogen atmosphere. After cooling down to ambient temperature, the resulting mixture was concentrated under reduced pressure and the residue was purified by silica gel column chromatography, eluted with 0~1% methanol in dichloromethane to afford **10** as an off-white solid (1.50 g, 88%): ^{1}H NMR (400 MHz, DMSO-d_6) δ 9.69 (s, 1H), 9.43 (s, 1H), 8.35-8.28 (m, 4H), 7.85-7.82 (m, 1H), 7.68 (d, J = 5.2 Hz, 1H), 7.61-7.56 (m, 1H), 6.89 (d, J = 3.9 Hz, 1H); LC/MS: $[(M+1)]^+ = 264.2$.

8-Fluoro-3-(1H-pyrrolo[2,3-c]pyridin-1-yl)isoquinoline (11):

Step 1. (*E*)-7Ffluoro-2-(hydroxyimino)-2,3-dihydro-1H-inden-1-one (11b): To a stirred solution of 7-fluoro-2,3-dihydro-1H-inden-1-one (**11a**) (2.0 g, 13.3 mmol) in diethyl ether (100 mL) was added a saturated solution of dry hydrochloride gas in methanol (10 mL) followed by the addition of isopentyl nitrite (2.3 g, 19.9 mmol) at 0 °C. After additional 1 hour, solids were collected by filtration and washed with diethyl ether (200 mL) to afford **11b** as a brown solid (1.5 g, 60%): ^{1}H NMR (300 MHz, DMSO-d_6) δ 12.75 (br s, 1H), 7.78-7.72 (m, 1H), 7.45-7.43 (m, 1H), 7.27-7.21 (m, 1H), 3.79 (s, 2H); LC/MS: $[(M+1)]^+ = 180.2$.

Step 2. 1,3-Dichloro-8-fluoroisoquinoline (11c): To a stirred solution of (E)-7-fluoro-2-(hydroxyimino)-2,3-dihydro-1H-inden-1-one (**11b**) (1.50 g, 8.37 mmol) in phosphorus oxytrichloride (20 mL, saturated with hydrochloride gas) was added pentachlorophosphorane (2.09 g, 10.05 mmol). The resulting mixture was stirred for 6 hours at 60 °C. After cooling down

to ambient temperature, the resulting mixture was concentrated under reduced pressure and the residue was triturated with water (100 mL) and filtered. The filter cake was washed with water (100 mL) and dried in a vacuum oven to afford **11c** as a brown solid (1.0 g, 53%): ^{1}H NMR (300 MHz, DMSO-d_6) δ 8.12 (s, 1H), 7.91-7.88 (m, 2H), 7.63-7.58 (m, 1H).

Step 3. 3-Chloro-8-fluoroisoquinoline (11d):   To a stirred solution of 1,3-dichloro-8-fluoroisoquinoline (**11c**) (1.0 g, 4.63 mmol) in acetic acid (30 mL) and hydriodic acid (15 mL, 55% w/w aqueous solution) was added red phosphorus (0.36 g, 11.57 mmol) at ambient temperature. The resulting mixture was stirred for 3 hours at 120 °C. After cooling down to ambient temperature, the resulting mixture was concentrated under reduced pressure. The residue was taken up by ethyl acetate (100 mL) and water (100 mL). The organic layer was separated out and the aqueous layer was extracted with ethyl acetate (2 x 100 mL). The combined organic layers was washed with brine (100 mL) and dried over anhydrous sodium sulfate. After filtration, the filtrate was concentrated under reduced pressure to afford 3-chloro-8-fluoroisoquinoline as a yellow solid (0.70 g, 79%): ^{1}H NMR (400 MHz, DMSO-d_6) δ 9.45 (s, 1H), 8.25 (s, 1H), 7.89-7.81 (m, 2H), 7.55-7.51 (m, 1H); LC/MS: $[(M +1)]^+$ = 182.2.

Step 4. 8-Fluoro-3-(1H-pyrrolo[2,3-c]pyridin-1-yl)isoquinoline (11): To a stirred solution of 1H-pyrrolo[2,3-c]pyridine (**8a**) (98.0 mg, 0.8 mmol) and 3-chloro-8-fluoroisoquinoline (**11d**) (100.0 mg, 0.6 mmol) in tetrahydrofuran (20 mL) was added sodium 2-methylpropan-2-olate (106.0 mg, 1.1 mmol) and t-BuXPhos palladium(II) biphenyl-2-amine mesylate (43.7 mg, 0.06 mmol) at ambient temperature. The resulting mixture was stirred for 12 hours at 50 °C under a nitrogen atmosphere. After cooling down to ambient temperature, the resulting mixture was diluted with water (30 mL) and extracted with ethyl acetate (3 x 30 mL). The combined organic layers was washed with brine (30 mL) and dried over anhydrous sodium sulfate. After filtration,

the filtrate was concentrated under reduced pressure and the residue was purified by silica gel column chromatography, eluted with 1~2% methanol in dichloromethane to afford **11** as an off-white solid (54.1 mg, 37%): ^{1}H NMR (300 MHz, DMSO-d_6) δ 9.74 (s, 1H), 9.56 (s, 1H), 8.39 (s, 2H), 8.30-8.27 (m, 1H), 7.93-7.83 (m, 2H), 7.69-7.68 (m, 1H), 7.47-7.43 (m, 1H), 6.90 (d, J = 3.3 Hz, 1H); LC/MS: $[(M +1)]^+$ = 264.2.

2-Fluoro-7-(1H-pyrrolo[2,3-c]pyridin-1-yl)-1,6-naphthyridine (12)

Step1. 5-Bromo-2-(1H-pyrrolo[2,3-c]pyridin-1-yl)isonicotinic acid (12b):   To a stirred solution of 1H-pyrrolo[2,3-c]pyridine (**8a**) (5.6 g, 47.9 mmol) in *N,N*-dimethylformamide (250 mL) were added cesium carbonate (46.8 g, 144.0 mmol) and methyl 5-bromo-2-chloroisonicotinate (**12a**) (12.0 g, 47.9 mmol). The resulting mixture was stirred for 16 hours at 80 °C. After cooling down to ambient temperature, solvent was evaporated out under reduced pressure and the residue was triturated with dichloromethane (500 mL). After filtration, the filter cake was collected, suspended in water (500 mL) and acidified by diluted hydrochloric acid (300 mL, 1N). A filtration was performed and the filter cake was collected and dried in the air to afford **12b** as a light yellow solid (10 g, 66%): ^{1}H NMR (300 MHz, DMSO-d^6) δ 14.70 (br s, 1H), 9.89 (s, 1H), 8.97-8.94 (m, 2H), 8.52 (d, J = 6.0 Hz, 1H), 8.28 (s, 1H), 8.23 (d, J = 6.3 Hz, 1H), 7.24 (d, J = 3.3 Hz, 1H); LC/MS: $[(M +1)]^+$ = 318.0, 320.0.

Step2. tert-Butyl (5-bromo-2-(1H-pyrrolo[2,3-c]pyridin-1-yl)pyridin-4-ylcarbamate (12c): To a stirred solution of 5-bromo-2-(1H-pyrrolo[2,3-c]pyridin-1-yl)isonicotinic acid (**12b**) (10.0 g, 31.4 mmol) and triethylamine (4.8 g, 47.2 mmol) in tert-butyl alcohol (250 mL) was added diphenyl phosphorazidate (26.0 g, 94.0 mmol) at ambient temperature. The resulting mixture was refluxed for 4 hours under a nitrogen atmosphere. After cooling down to ambient temperature,

the resulting mixture was concentrated under reduced pressure and the residue was purified by silica gel column chromatography, eluted with 2~10% methanol in dichloromethane to afford **12c** as a light yellow solid (3.0 g, 25%): ^{1}H NMR (300 MHz, DMSO-d^6) δ 9.56 (br s, 1H), 8.95 (s, 1H), 8.69 (s, 1H), 8.29 (d, J = 5.4 Hz, 1H), 8.20 (s, 1H), 8.18 (d, J = 3.3 Hz, 1H), 7.69 (d, J = 5.1 Hz, 1H), 6.87 (d, J = 3.3 Hz, 1H), 1.53 (s, 9H).

Step 3. 5-Bromo-2-(1H-pyrrolo[2,3-c]pyridin-1-yl)pyridin-4-amine (12d): A solution of tert-butyl (5-bromo-2-(1H-pyrrolo[2,3-c]pyridin-1-yl)pyridin-4-yl)carbamate (**12c**) (0.70 g, 1.79 mmol) in dichloromethane (32 mL) was treated with trifluoroacetic acid (4 mL) at ambient temperature for 3 hours. The resulting solution was concentrated under reduced pressure and the residue was dissolved into dichloromethane (50 mL), washed with saturated aqueous solution of sodium bicarbonate (2 x 50 mL). The organic layer was dried over anhydrous sodium sulfate and filtered. The filtrate was concentrated under reduced pressure and the residue was purified by silica gel column chromatography, eluted with 1~10% methanol in dichloromethane to afford **12d** as a light yellow solid (0.50 g, 91%): ^{1}H NMR (300 MHz, DMSO-d^6) δ 9.46 (br s, 1H), 8.29 (s, 1H), 8.25 (d, J = 5.4 Hz, 1H), 8.04 (d, J = 3.3 Hz, 1H), 7.64 (d, J = 5.4 Hz, 1H), 7.04 (s, 1H), 6.78 (d, J = 3.3 Hz, 1H), 6.63 (br s, 2H); LC/MS: [(M +1)]$^+$ = 289.0, 291.0.

Step4. (*E*)-Ethyl 3-(4-amino-6-(1H-pyrrolo[2,3-c]pyridin-1-yl)pyridin-3-yl)acrylate (12e): To a solution of 5-bromo-2-(1H-pyrrolo[2,3-c]pyridin-1-yl)pyridin-4-amine (**12d**) (1.0 g, 3.46 mmol) in *N,N*-dimethylformamide (50 mL) were added ethyl acrylate (1.38 g, 13.83 mmol), triethylamine (1.40 g, 13.83 mmol), palladium (II) acetate (0.078 g, 0.35 mmol) and tri-o-tolylphosphine (0.21 g, 0.69 mmol) at ambient temperature under nitrogen atmosphere. The resulting solution was stirred for 16 hours at 120 °C. After cooling down to ambient temperature, the resulting mixture was concentrated under reduced pressure and the residue was purified by

silica gel column chromatography, eluted with 1~3% methanol in dichloromethane to afford **12e** as a light yellow solid (0.7 g, 66%): ^{1}H NMR (300 MHz, DMSO-d^6) δ 9.65 (s, 1H), 8.56 (s, 1H), 8.36-8.32 (m, 2H), 7.94-7.83 (m, 2H), 6.97 (t, *J* = 4.2 Hz, 2H), 6.90 (br s, 2H), 6.60 (d, *J* = 15.9 Hz, 1H), 4.21 (q, *J* = 7.8 Hz, 2H), 1.21 (t, *J* = 7.8 Hz, 3H); LC/MS: [(M +1)]$^+$ = 309.2.

Step5. 7-(1H-Pyrrolo[2,3-c]pyridin-1-yl)-1,6-naphthyridin-2(1H)-one (12f): A solution of (*E*)-ethyl 3-(4-amino-6-(1H-pyrrolo[2,3-c]pyridin-1-yl)pyridin-3-yl)acrylate (**12e**) (150 mg, 0.49 mmol) in ethanol (5 mL) was treated with sodium ethanolate (166 mg, 2.43 mmol) for 1 hour at 78 °C. After cooling down to ambient temperature, the reaction was quenched by water (5 mL) and neutralized with acetic acid (0.2 mL). The resulting mixture was concentrated under reduced pressure and the residue was purified by silica gel column chromatography, eluted with 1~5% methanol in dichloromethane to afford **12f** as an off white solid (100 mg, 78 %): ^{1}H NMR (300 MHz, DMSO-d^6) δ 12.15 (br s, 1H), 9.59 (s, 1H), 8.89 (s, 1H), 8.31 (d, *J* = 5.4 Hz, 1H), 8.18 (d, *J* = 3.6 Hz, 1H), 8.05 (d, *J* = 9.6 Hz, 1H), 7.69 (d, *J* = 4.8 Hz, 1H), 7.49 (s, 1H), 6.88 (d, *J* = 3.3 Hz, 1H), 6.55 (d, *J* = 9.3 Hz, 1H); LC/MS: [(M +1)]$^+$ = 263.1.

Step 6. 2-Chloro-7-(1H-pyrrolo[2,3-c]pyridin-1-yl)-1,6-naphthyridine (12g):   A solution of 7-(1H-pyrrolo[2,3-c]pyridin-1-yl)-1,6-naphthyridin-2(1H)-one (**12f**) (100 mg, 0.38 mmol) in trichloro phosphorous oxide (5 mL) was stirred for 1 hour at 80 °C. After cooling down to ambient temperature, the resulting mixture was concentrated under reduced pressure and the residue was taken up into water (20 mL) and neutralized with saturated aqueous solution of sodium bicarbonate (2 mL). The resulting mixture was concentrated under reduced pressure and the residue was purified by silica gel column chromatography, eluted with 2~3% methanol in dichloromethane to afford **12g** as an off white solid (90 mg, 84%): ^{1}H NMR (300 MHz, DMSO-

d^6) δ 9.85 (s, 1H), 9.55 (s, 1H), 8.71 (d, J = 8.4 Hz, 1H), 8.50 (d, J = 3.3 Hz, 1H), 8.32-8.28 (m, 2H), 7.72-7.61 (m, 2H), 6.93 (d, J = 3.3 Hz, 1H); LC/MS: [(M +1)][+] = 281.1.

Step 7. 2-Fluoro-7-(1H-pyrrolo[2,3-c]pyridin-1-yl)-1,6-naphthyridine (12): A mixture of 2-chloro-7-(1H-pyrrolo[2,3-c]pyridin-1-yl)-1,6-naphthyridine (**12g**) (100 mg, 0.36 mmol) and potassium fluoride (62 mg, 1.07 mmol) in dimethylsulfoxide (3 mL) was irradiated with microwave (100 W) for 1 hour at 120 ^{o}C. After cooling down to ambient temperature, a filtration was performed and the filtrate was purified by Prep-HPLC with the following condition: [Column: X Bridge C18, 19 * 150 mm, 5 um; Mobile Phase A: Water (plus 0.1% TFA, w/w), Mobile Phase B: MeOH; Flow rate: 20 mL/min; Gradient: 60%~80% B in 10 min; Detector 254 nm;] to afford **12** as an off white solid (61 mg, 61%, RT: 6.3 min): ^{1}H NMR (300 MHz, DMSO-d^6) δ 10.08 (s, 1H), 9.59 (s, 1H), 9.16 (d, J = 3.3 Hz, 1H), 8.96 (t, J = 8.7 Hz, 1H), 8.56-8.51 (m, 2H), 8.30 (t, J = 9.0 Hz, 1H), 7.61-7.58 (m, 1H), 7.34 (d, J = 3.6 Hz, 1H); LC/MS: [(M +1)][+] = 265.1.

ASSOCIATED CONTENT

Supporting Information. Radiosynthesis experimental procedures, in vitro and in vivo assay and imaging protocols are included in the Supporting Information. This material is available free of charge via the Internet at http://pubs.acs.org.

AUTHOR INFORMATION

Corresponding Author

*E-mail: abbas_walji@merck.com. Phone: (215)-652-3379

ABBREVIATIONS

AD, Alzheimer's disease; PET, positron emission tomography,; NFT, neurofibrillary tangle, sfLogD, shake flake Log D; SUV, standard uptake value; GM, gery matter; WM, white matter; IHC, immunohistochemistry; CNS-MPO, central nervous system-multiparameter optimization; BBB, blood brain barrier.

REFERENCES

1.	Hampel, H.; Frank, R.; Broich, K.; Teipel, S. J.; Katz, R. G.; Hardy, J.; Herholz, K.; Bokde, A. L. W.; Jessen, F.; Hoessler, Y. C.; Sanhai, W. R.; Zetterberg, H.; Woodcock, J.; Blennow, K. Biomarkers for Alzheimer's Disease: Academic, Industry and Regulatory perspectives. . *Nat. Rev. Drug Discovery* **2010,** *9*, 560-574.

2.	Jack, C. R.; Holtzman, D. M. Biomarker Modeling of Alzheimer's Disease. *Neuron* **2013,** *80*, 1347-1358.

3.	Jagust, W. J.; Landau, S. M.; Koeppe, R. A.; Reiman, E. M.; Chen, K. W.; Mathis, C. A.; Price, J. C.; Foster, N. L.; Wang, A. Y. The Alzheimer's Disease Neuroimaging Initiative 2: PET core: 2015. *Alzheimer's Dementia* **2015,** *11*, 757-771.

4.	Frank, R.; Hargreaves, R. Clinical Biomarkers in Drug Discovery and Development. *Nat. Rev. Drug Discovery* **2003,** *2*, 566-580.

5.   Lista, S.; O'Bryant, S. E.; Blennow, K.; Dubois, B.; Hugon, J.; Zetterberg, H.; Hampel, H. Biomarkers in Sporadic and Familial Alzheimer's Disease. *J. Alzheimer's Dis.* **2015,** *47*, 291-317.

6.   Rowe, C. C.; Ng, S.; Ackermann, U.; Gong, S. J.; Pike, K.; Savage, G.; Cowie, T. F.; Dickinson, K. L.; Maruff, P.; Darby, D.; Smith, C.; Woodward, M.; Merory, J.; Tochon-Danguy, H.; O'Keefe, G.; Klunk, W. E.; Mathis, C. A.; Price, J. C.; Masters, C. L.; Villemagne, V. L. Imaging β-Amyloid Burden in Aging and Dementia. *Neurology* **2007,** *68*, 1718-1725.

7.   Thompson, P. W.; Ye, L.; Morgenstern, J. L.; Sue, L.; Beach, T. G.; Judd, D. J.; Shipley, N. J.; Libri, V.; Lockhart, A. Interaction of the Amyloid Imaging Tracer [^{18}F]-DDNP with Hallmark Alzheimer's Disease Pathologies. *J. Neurochem.* **2009,** *109*, 623-630.

8.   Serdons, K.; Verduyckt, T.; Vanderghinste, D.; Cleynhens, J.; Borghgraef, P.; Vermaelen, P.; Terwinghe, C.; Van Leuven, F.; Van Laere, K.; Kung, H.; Bormans, G.; Verbruggen, A. Synthesis of F-18-Labelled 2-(4 '-fluorophenyl)-1,3-benzothiazole and Evaluation as Amyloid Imaging Agent in Comparison with C-11 PIB. *Bioorg. Med. Chem. Lett.* **2009,** *19*, 602-605.

9.   Eckroat, T. J.; Mayhoub, A. S.; Garneau-Tsodikova, S. Amyloid-β Probes: Review of Structure-Activity and Brain-Kinetics Relationships. *Beilstein J. Org. Chem.* **2013,** *9*, 1012-1044.

10.   Rowe, C. C.; Villemagne, V. L. Amyloid Imaging with PET in Early Alzheimer Disease Diagnosis. *Med. Clin. North Am.* **2013,** *97*, 377-398.

11.   Kepe, V.; Moghbel, M. C.; Langstrom, B.; Zaidi, H.; Vinters, H. V.; Huang, S.-C.; Satyamurthy, N.; Doudet, D.; Mishani, E.; Cohen, R. M.; Hoilund-Carlsen, P. F.; Alavi, A.;

Barrio, J. R. Amyloid-β Positron Emission Tomography Imaging Probes: A Critical Review. *J. Alzheimer's Dis.* **2013,** *36*, 613-631.

12.   Landau, S. M.; Thomas, B. A.; Thurfjell, L.; Schmidt, M.; Margolin, R.; Mintun, M.; Pontecorvo, M.; Baker, S. L.; Jagust, W. J.; Alzheimer's Dis Neuroimaging, I. Amyloid PET Imaging in Alzheimer's Disease: A Comparison of Three Radiotracers. *Eur. J. Nucl. Med. Mol. Imaging* **2014,** *41*, 1398-1407.

13.   Bolaender, A.; Kieser, D.; Voss, C.; Bauer, S.; Schoen, C.; Burgold, S.; Bittner, T.; Hoelzer, J.; Heyny-von Haussen, R.; Mall, G.; Goetschy, V.; Czech, C.; Knust, H.; Berger, R.; Herms, J.; Hilger, I.; Schmidtt, B. Bis(arylvinyl)pyrazines, -pyrimidines, and -pyridazines as Imaging Agents for Tau Fibrils and β-Amyloid Plaques in Alzheimer's Disease Models. *J. Med. Chem.* **2012,** *55*, 9170-9180.

14.   Harrison, S. T.; Mulhearn, J.; Wolkenberg, S. E.; Miller, P. J.; O'Malley, S. S.; Zeng, Z.; Williams, D. L., Jr.; Hostetler, E. D.; Sanabria-Bohorquez, S.; Gammage, L.; Fan, H.; Sur, C.; Culberson, J. C.; Hargreaves, R. J.; Cook, J. J.; Hartman, G. D.; Barrow, J. C. Synthesis and Evaluation of 5-fluoro-2-aryloxazolo 5,4-b pyridines as β-Amyloid PET Ligands and Identification of MK-3328. *ACS Med. Chem. Lett.* **2011,** *2*, 498-502.

15.   Arriagada, P. V.; Growdon, J. H.; Hedleywhyte, E. T.; Hyman, B. T. Neurofibrillary Tangles but not Senile Plaques Parallel Duration and Severity of Alzheimer's-Disease. *Neurology* **1992,** *42*, 631-639.

16.   Andreadis, A.; Brown, W. M.; Kosik, K. S. Structure and Novel Exons of the Human-Tau Gene. *Biochemistry* **1992,** *31*, 10626-10633.

17.   Buee, L.; Bussiere, T.; Buee-Scherrer, V.; Delacourte, A.; Hof, P. R. Tau Protein Isoforms, Phosphorylation and Role in Neurodegenerative Disorders. *Brain Res. Rev.* **2000,** *33*, 95-130.

18.   Buee, L.; Hamdane, M.; Delobel, P.; Bussiere, T.; Sergeant, N.; Delacourte, A. Role of Tau in Alzheimer's Disease and Other Tauopathies. *Mov. Disord.* **2002,** *17*, 1407-1407.

19.   Maccioni, R. B.; Farias, G.; Morales, I.; Navarrete, L. The Revitalized Tau Hypothesis on Alzheimer's Disease. *Arch. Med. Res.* **2010,** *41*, 226-231.

20.   Spillantini, M. G.; Goedert, M. Tau Pathology and Neurodegeneration. *Lancet Neurol.* **2013,** *12*, 609-622.

21.   Alafuzoff, I.; Arzberger, T.; Al-Sarraj, S.; Bodi, I.; Bogdanovic, N.; Braak, H.; Bugiani, O.; Del-Tredici, K.; Ferrer, I.; Gelpi, E.; Giaccone, G.; Graeber, M. B.; Ince, P.; Kamphorst, W.; King, A.; Korkolopoulou, P.; Kovacs, G. G.; Larionov, S.; Meyronet, D.; Monoranu, C.; Parchi, P.; Patsouris, E.; Roggendorf, W.; Seilhean, D.; Tagliavini, F.; Stadelmann, C.; Streichenberger, N.; Thal, D. R.; Wharton, S. B.; Kretzschmar, H. Staging of Neurofibrillary Pathology in Alzheimer's Disease: A Study of the Brainnet Europe Consortium. *Brain Pathol.* **2008,** *18*, 484-496.

22.   Braak, H.; Braak, E. Frequency of Stages of Alzheimer-Related Lesions in Different Age Categories. *Neurobiol. Aging* **1997,** *18*, 351-357.

23.   Delacourte, A.; David, J. P.; Sergeant, N.; Buee, L.; Wattez, A.; Vermersch, P.; Ghozali, F.; Fallet-Bianco, C.; Pasquier, F.; Lebert, F.; Petit, H.; Di Menza, C. The Biochemical Pathway of Neurofibrillary Degeneration in Aging and Alzheimer's Disease. *Neurology* **1999,** *52*, 1158-1165.

24. Villemagne, V. L.; Fodero-Tavoletti, M. T.; Masters, C. L.; Rowe, C. C. Tau Imaging: Early Progress and Future Directions. *Lancet Neurol.* **2015,** *14*, 114-124.

25. Ariza, M.; Kolb, H. C.; Moechars, D.; Rombouts, F.; Andres, J. I. Tau Positron Emission Tomography (PET) Imaging: Past, Present, and Future. *J. Med. Chem.* **2015,** *58*, 4365-4382.

26. Shah, M.; Catafau, A. M. Molecular Imaging Insights into Neurodegeneration: Focus on Tau PET Radiotracers. *J. Nucl. Med.* **2014,** *55*, 871-874.

27. Mathis, C. A.; Klunk, W. E. Imaging Tau Deposits In Vivo: Progress in Viewing more of the Proteopathy Picture. *Neuron* **2013,** *79*, 1035-1037.

28. Villemagne, V. L.; Okamura, N. In Vivo Tau Imaging: Obstacles and Progress. *Alzheimer's Dementia* **2014,** 10, S254-S264.

29. James, O. G.; Doraiswamy, P. M.; Borges-Neto, S. PET Imaging of Tau Pathology in Alzheimer's Disease and Tauopathies. *Front. Neurol.* **2015,** *6*, 1-4.

30. Okamura, N.; Harada, R.; Furumoto, S.; Arai, H.; Yanai, K.; Kudo, Y. Tau PET Imaging in Alzheimer's Disease. *Curr. Neurol. Neurosci. Rep.* **2014,** *14*, 1-7

31. Mintun, M.; Devous, M., Sr.; Attardo, G.; Joshi, A.; Schwarz, A.; Shcherbinin, S.; Siderowf, A.; Lin, Y. G.; Liang, Q.; Conway, K.; Gomez, F.; Pontecorvo, M. Potential Utility of the Tau Deposit Tracer [^{18}F]-T807 (aka [^{18}F]-AV-1451) as a PET Biomarker for Neurodegeneration in Clinical Trials. *Neuropsychopharmacology* **2014,** 39, S207-S208.

32. Pontecorvo, M.; Devous, M.; Joshi, A.; Lu, M.; Siderowf, A.; Arora, A.; Mintun, M. Relationships Between [^{18}F]-AV-1451 (aka [^{18}F]-T807) PET Tau Binding and Amyloid Burden in Cognitively Normal Subjects and Patients with Cognitive Impairments Suspected of Alzheimer's Disease. Abstract Number 245. *J. Nucl. Med.* **2015,** *56*, Suppl; abstr 245.

33.   Chien, D. T.; Bahri, S.; Szardenings, A. K.; Walsh, J. C.; Mu, F.; Su, M.-Y.; Shankle, W. R.; Elizarov, A.; Kolb, H. C. Early Clinical PET Imaging Results with the Novel PHF-Tau Radioligand [^{18}F]-T807. *J. Alzheimer's Dis.* **2013,** 34, 457-468.

34.   Xia, C.-F.; Arteaga, J.; Chen, G.; Gangadharmath, U.; Gomez, L. F.; Kasi, D.; Lam, C.; Liang, Q.; Liu, C.; Mocharla, V. P.; Mu, F.; Sinha, A.; Su, H.; Szardenings, A. K.; Walsh, J. C.; Wang, E.; Yu, C.; Zhang, W.; Zhao, T.; Kolb, H. C. [^{18}F]-T807, A Novel Tau Positron Emission Tomography Imaging Agent for Alzheimer's Disease. *Alzheimer's Dementia* **2013,** 9, 666-676.

35.   Chien, D. T.; Szardenings, A. K.; Bahri, S.; Walsh, J. C.; Mu, F.; Xia, C.; Shankle, W. R.; Lerner, A. J.; Su, M.-Y.; Elizarova, A.; Kolb, H. C. Early Clinical PET Imaging Results with the Novel PHF-Tau Radioligand F18-T808. *J. Alzheimer's Dis.* **2014,** 38, 171-184.

36.   Brendel, M.; Okamura, N.; Jaworska, A.; Lindner, S.; Roetzer, C.; Herms, J.; Bartenstein, P.; Rominger, A. PET Imaging of Tau Pathology in a Transgenic Mouse Model Using [^{18}F]-THK-5117. Abstract Number 28. *J. Nucl. Med.* **2014,** *55*, Suppl; abstr 28.

37.   Harada, R.; Okamura, N.; Furumoto, S.; Furukawa, K.; Ishiki, A.; Tomita, N.; Hiraoka, K.; Watanuki, S.; Shidahara, M.; Miyake, M.; Ishikawa, Y.; Matsuda, R.; Inami, A.; Yoshikawa, T.; Tago, T.; Funaki, Y.; Iwata, R.; Tashiro, M.; Yanai, K.; Arai, H.; Kudo, Y. [^{18}F]-THK-5117 PET for Assessing Neurofibrillary Pathology in Alzheimer's Disease. *Eur. J. Nucl. Med. Mol. Imaging* **2015,** *42*, 1052-1061.

38.   Ishiki, A.; Okamura, N.; Furukawa, K.; Furumoto, S.; Harada, R.; Tomita, N.; Hiraoka, K.; Watanuki, S.; Ishikawa, Y.; Tago, T.; Funaki, Y.; Iwata, R.; Tashiro, M.; Yanai, K.; Kudo, Y.; Arai, H. Longitudinal Assessment of Tau Pathology in Patients with Alzheimer's Disease Using [^{18}F]-THK-5117 Positron Emission Tomography. *PLoS One* **2015,** *10*, 1-9.

39. Okamura, N.; Furumoto, S.; Harada, R.; Tago, T.; Iwata, R.; Tashiro, M.; Furukawa, K.; Arai, H.; Yanai, K.; Kudo, Y. Characterization of [^{18}F]-THK-5351, A Novel PET Tracer for Imaging Tau Pathology in Alzheimer's Disease. Abstract Number 260. *Eur. J. Nucl. Med. Mol. Imaging* **2014,** *41*, Suppl; abstr 260.

40. Ito, H.; Shimada, H.; Ikoma, Y.; Shinotoh, H.; Kimura, Y.; Ichise, M.; Suhara, T.; Higuchi, M. Quantitative Analysis of Tau Pathology in Human Brain Using PET with C-11 PBB3. *J. Nucl. Med.* **2015,** *56*, 136.

41. Wang, M.; Gao, M.; Xu, Z.; Zheng, Q.-H. Synthesis of a PET Tau Tracer C-11 PBB3 for Imaging of Alzheimer's Disease. *Bioorg. Med. Chem. Lett.* **2015,** *25*, 4587-4592.

42. Gandy, S.; DeKosky, S. T. [^{18}F]-T807 Tauopathy PET Imaging in Chronic Traumatic Encephalopathy. *F1000Research* **2014,** *3*, 229.

43. Marquie, M.; Normandin, M. D.; Vanderburg, C. R.; Costantino, I. M.; Bien, E. A.; Rycyna, L. G.; Klunk, W. E.; Mathis, C. A.; Ikonomovic, M. D.; Debnath, M. L.; Vasdev, N.; Dickerson, B. C.; Gomperts, S. N.; Growdon, J. H.; Johnson, K. A.; Frosch, M. P.; Hyman, B. T.; Gomez-Isla, T. Validating Novel Tau Positron Emission Tomography Tracer [^{18}F]-AV-1451 (T807) on postmortem brain tissue. *Ann. Neurol.* **2015,** *78*, 787-800.

44. Vermeiren, C.; Mercier, J.; Viot, D.; Mairet-Coello, G.; Hannestad, J.; Courade, J.-P.; Citron, M.; Gillard, M. T807, A Reported Selective Tau Tracer, Binds with Nanomolar Affinity to Monoamine Oxidase A. Abstract Number 283. *Alzheimer's Dementia* **2015,** *11*, Suppl; abstr 283.

45. Tarcsay, A.; Keseru, G. M. Contributions of Molecular Properties to Drug Promiscuity Miniperspective. *J. Med. Chem.* **2013,** *56*, 1789-1795.

46.   Hopkins, A. L.; Keserue, G. M.; Leeson, P. D.; Rees, D. C.; Reynolds, C. H. The Role of Ligand Efficiency Metrics in Drug Discovery. *Nat. Rev. Drug Discovery* **2014,** *13*, 105-121.

47.   Murray, C. W.; Erlanson, D. A.; Hopkins, A. L.; Keserue, G. M.; Leeson, P. D.; Rees, D. C.; Reynolds, C. H.; Richmond, N. J. Validity of Ligand Efficiency Metrics. *ACS Med. Chem. Lett.* **2014,** *5*, 616-618.

48.   Wager, T. T.; Hou, X.; Verhoest, P. R.; Villalobos, A. Moving Beyond Rules: The Development of a Central Nervous System Multiparameter Optimization (CNS-MPO) Approach to Enable Alignment of Druglike Properties. *ACS Chem. Neurosci.* **2010,** *1*, 435-449.

49.   Hostetler, E.; Sanabria-Bohorquez, S.; Fan, H.; Zeng, Z.; Williams, D.; O'Malley, S.; Miller, P.; Chen, T.-B.; Culberson, C.; Daneker, L.; Harrison, S.; Mulhearn, J.; Wolkenberg, S.; Barrow, J.; Hargreaves, R.; Sur, C.; Cook, J. [^{18}F]-MK-3328: Evaluation of a Novel PET Tracer for Amyloid Plaque in Rhesus Monkey. *NeuroImage* **2010,** *52*, S154.

50.   Walji, A. M.; Hostetler, E.; Greshock, T.; Li, J.; Moore, K. P.; Bennacef, I.; Mulhearn, J.; Selnick, H.; Wang, Y.; Yang, K.; Fu, J. Pyrrolo[2,3-c]pyridines as Imaging Agents for Neurofibrilary Tangles. WO2015191506A2, 2015.

51.   Innis, R. B.; Cunningham, V. J.; Delforge, J.; Fujita, M.; Giedde, A.; Gunn, R. N.; Holden, J.; Houle, S.; Huang, S.-C.; Ichise, M.; Lida, H.; Ito, H.; Kimura, Y.; Koeppe, R. A.; Knudsen, G. M.; Knuuti, J.; Lammertsma, A. A.; Laruelle, M.; Logan, J.; Maguire, R. P.; Mintun, M. A.; Morris'o, E. D.; Parsey, R.; Price, J. C.; Slifstein, M.; Sossi, V.; Suhara, T.; Votaw, J. R.; Wong, D. F.; Carson, R. E. Consensus Nomenclature for In Vivo Imaging of Reversibly Binding Radioligands. *J. Cereb. Blood Flow Metab.* **2007,** *27*, 1533-1539.

1
2
3
4
5
6
7
8
9
10
11
12
13
14
15
16
17
18
19
20
21
22
23
24
25
26
27
28
29
30
31
32
33
34
35
36
37
38
39
40
41
42
43
44
45
46
47
48
49
50
51
52
53
54
55
56
57
58
59
60

Table of Contents Graphic:

9
NFT K_i = 8.8 nM
Minimal Pharmacophore

Lead Optimization

[^{18}F]6
NFT K_i = 0.36 nM
Clinical Candidate

Non-Human Primate PET Imaging Studies

[^{18}F]6 Baseline   [^{18}F]6 after 1 mg/kg 6